Please fill in the name of the event you are preparing this manuscript for.	SPE Hydraulic Fracturing Technology Conference and Exhibition
Please fill in your 6-digit SPE manuscript number.	SPE-212376-MS
Please fill in your manuscript title.	Real-Time Monitoring of Fracture Dynamics with a Contrast Agent-Assisted Electromagnetic Method

Please fill in your author name(s) and company affiliation.

Given Name	Surname	Company
Mohsen	Ahmadian	Bureau of Economic Geology, The University of Texas at Austin
Mahdi	Haddad	Bureau of Economic Geology, The University of Texas at Austin
Liangze	Cui	Duke University
Alfred	Kleinhammes	University of North Carolina
Patrick	Doyle	University of North Carolina
Jeffrey	Chen	DIT, ESG Solutions
Trevor	Pugh	DIT, ESG Solutions
Qing Huo	Liu	Duke University
Yue	Wu	University of North Carolina
Darwin	Mohajeri	Bureau of Economic Geology, The University of Texas at Austin

Abstract

In collaboration with the Advanced Energy Consortium, our team has previously demonstrated that the placement of electrically active proppants (EAPs) in a hydraulic fracture surveyed by electromagnetic (EM) methods can enhance the imaging of the stimulated reservoir volumes during hydraulic fracturing. That work culminated in constructing a well-characterized EAP-filled fracture anomaly at the Devine field pilot site (DFPS). In subsequent laboratory studies, we observed that the electrical conductivity of our EAP correlates with changes in pressure, salinity, and flow. Thus, we postulated that the EAP could be used as an *in-situ* sensor for the remote monitoring of these changes in previously EAP-filled fractures. This paper presents our latest field data from the DFPS to demonstrate such correlations at an intermediate pilot scale.

We conducted surface-based EM surveys during freshwater (200 ppm) and saltwater (2,500 ppm) slug injections while running surfaced-based EM surveys. Simultaneously, we measured the following: 1) bottomhole pressure and salinity in five monitoring wells; 2) injection rate using high-precision data loggers; 3) distributed acoustic sensors in four monitoring wells; and 4) tiltmeter data on the survey area.

We demonstrated that injections into an EAP-filled fracture could be successfully coupled with real-time electric field measurements on the surface, leading to remote monitoring of dynamic

changes within the EAP-filled fracture. Furthermore, by comparing the electrical field traces with the bottomhole pressure, flow rate, and salinity, we concluded that the observed electric field in our study is influenced by fracture dilation and flow rate. Salinity effect was observed when saltwater was injected. EM simulations solely based on assumptions of fracture conductivity changes during injection did not reproduce all of the measured electric field magnitudes. Preliminary estimates showed that including streaming potential in our geophysical model may be needed to reduce the simulation mismatch.

The methods developed and demonstrated during this study will lead to a better understanding of the extent of fracture networks, formation stress states, fluid leakoff and invasion, characterizations of engineered fracture systems, and other applications where monitoring subsurface flow tracking is deemed important.

Keywords

Electrically active proppant, Electromagnetic geophysics, Devine field pilot site, *in-situ* sensor, Stimulated reservoir volume, Hydraulic fracturing, Fracture dynamics

Introduction

Multistage hydraulic fracture stimulations along horizontal wells have offered an economical solution for production from unconventional reservoirs in the past 20 years. Understanding the hydraulic-fracture dimensions is critical for long-term production estimation that cannot be achieved only through near-well diagnostic techniques. On the other hand, far-field diagnostic surveys such as electromagnetic tomography have been developed to characterize hydraulic fractures at far distances from horizontal wells (Heagy et al., 2014; Denison et al., 2015; Hu et al., 2016, 2018; LaBrecque et al., 2016; Ahmadian et al., 2018, 2019; Fang et al., 2019; Stolyarov et al., 2019). This tomography has been enhanced by the placement of electrically active proppants (EAPs) in the hydraulic fracture (LaBrecque et al., 2016; Hu et al., 2018; Ahmadian et al., 2018, 2019). In other studies, electrical tomography of a hydraulic fracture has been acquired based on conductivity changes due to the injection of large fracturing fluid volumes (Haustveit et al., 2017; Zhang et al., 2021). Electromagnetic imaging has been successfully applied in other applications such as pore fluid flow monitoring (Spies, 1992; Nobes, 1996; Hu et al., 2016), engineered geothermal systems (Munoz, 2014), and carbon capture and sequestration (Zhdanov et al., 2013). Mizunaga and Tanaka (2015) adopted the electromagnetic method induced by the streaming potential (SP) to visualize fluid flow in a geothermal field.

To evaluate the performance of EAPs in assisting with the geophysical tomography of hydraulic fracture networks, the DFPS in Medina County, Texas, was previously completed and instrumented by the Advanced Energy Consortium (AEC). In those studies, a shallow hydraulic fracture was initiated from perforations at 175 ft depth. An EM inversion model predicted that this horizontal hydraulic fracture was almost horizontal (Ahmadian et al., 2018). Then, Ahmadian et al. (2019) validated this observation through drilling, coring, and logging of several wellbores within the interpreted fracture zone and developed models to predict the ground truth observations. In addition, multiple induction logs acquired from various validation wells outside and inside the

fracture area showed a large variation in conductivity at 175 ft depth, inferring proppant screenout. Furthermore, that study validated the boundaries of the EAP-filled fracture with a precision of approximately 5 feet from the model predictions (Ahmadian et al., 2019).

In the current follow-up study, we have attempted to demonstrate the applicability of the previously emplaced EAP pack in mapping hydraulic-fracture reopening or fluid diffusion and flow through the same well-characterized hydraulic fracture at the DFPS. For this purpose, we conducted multiple injection experiments consisting of freshwater and saltwater slug injections while running surfaced-based EM surveys. Simultaneously, we collected bottomhole pressure and salinity, injection flow rate, and surface pressure using high-precision data loggers, distributed acoustic sensing (DAS) data in various monitoring wells, and tiltmeter data in the survey area. This paper discusses a preliminary analysis of collected data by reviewing changes in the surface electric field amplitude and phase in conjunction with the injection flow rate, bottomhole pressure, and salinity profiles.

Lab Observations

This field study was prompted by our lab studies of the electrical responses of EAPs to pore fluid pressure changes. These studies suggested that the connectivity of electrically conductive proppants within a fracture can change significantly during fluid injection due to pressure changes and fluid flow. The conductivity of the fracture is sensitive to the changes in the contact area between grains. Granular compaction reduces contact resistance and increases the electrical conductivity of the pack. Injection pressures that exceed any external compacting pressures can lead to grain separation and a significant reduction in the overall conductivity.

Fig. 1 shows a schematic diagram and the experimental setup used to measure the conductivity of an EAP pack during fluid injection. During this study, a column of water-saturated EAPs was placed under a simulated overburden (lithostatic) pressure and subjected to several horizontal fluid injections to increase the hydrostatic pore pressure. In this proof-of-concept experiment, which mimics the DFPS setup, the fluid injection was carried out manually using a syringe while the impedance was monitored over time. Injections at various pressures were applied successively for finite amounts of time to observe the system response to pressure changes during four-time intervals, as shown on the right in **Fig. 1**. These time intervals represent: 1) discrete overburden pressure increase; 2) water injection at low pressures; 3) high-pressure injection; and 4) the highest-pressure injection to overcome the overburden pressure. Conductivity was derived from the measured complex impedance obtained from a four-electrode spectroscopy analyzer, ranging from approximately 0 to 350 S/m.

During time interval 1, increasing the overburden pressure alone resulted in an increase in conductivity from 300 to 350 S/m due to further grain compaction. In time interval 2, the low-pressure water injections reduced grain-to-grain contact and caused a slight conductivity drop. During time intervals 3 and 4, injections were conducted at larger pressures, followed each time by pressure release. These high-pressure injections led to further reductions in conductivity due to grain separation. Subsequently, a rebound in conductivity was observed when the pressure was released. We attribute this change to the re-establishment of the grain contact area. In time interval

4, a fluid pressure is applied that exceeds the overburden pressure. The uplift of the overburden weight reduces grain contact and drops the conductivity to a low value of less than 1 S/m. Again, after the pressure release, the conductivity rebounds to a value close to what was observed before the fluid injection. The higher conductivity is attributed to the piston slamming into the proppant pack, creating greater connectivity between grains and, thus, higher conductivity within the EAP pack.

These experiments clarified that the changes in conductivity could be attributed to changes in the intergranular contact area. The most dramatic changes occur when the injection pressure exceeds the overburden pressure, causing the connectivity between grains to weaken significantly and the resistivity to increase precipitously. High conductivity is reestablished within the proppant layer when the injection pressure is subsequently reduced. These laboratory scenarios simulate injection schedules in real fracture systems during which the fracture aperture is dilated or closed.

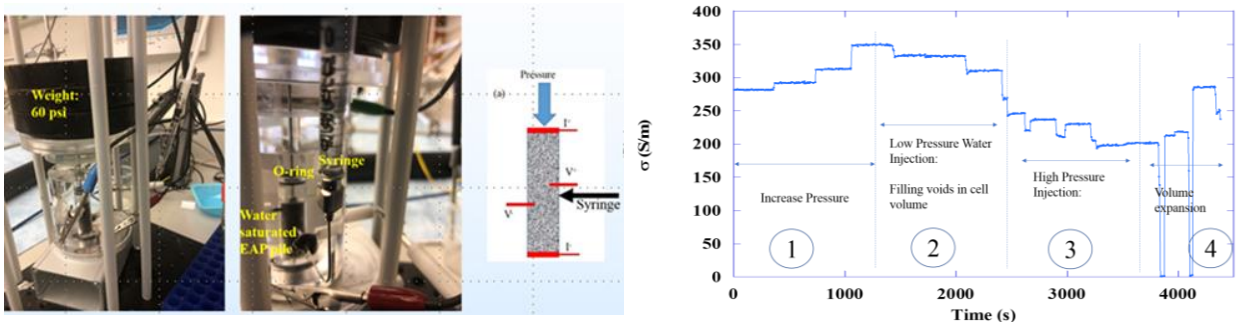

Fig. 1—Conductivity response to pressure changes, tested using side-port water injections into a water-saturated EAP granular pack under the overburden pressure. (left) Experimental setup. (middle) A schematic of the design. (right) Conductivity versus time. The conductivity is determined from a four-electrode impedance measurement. The effect of overburden pressure and the injected water pressure was investigated qualitatively by the stepwise increases in the overburden pressure and by fluid injections during four-time intervals.

We conducted similar tests using a sand pack consisting of nonelectrically conductive grains. These sand-pack tests resulted in negligible relative conductivity changes with pressure changes compared to significant conductivity changes of an EAP pack due to the same pressure changes. Based on these results, we postulated that the surface-deployed EM methods could be used in remote sensing of *in situ* alterations of physical properties of an EAP-filled fracture at the DFPS. We assumed that the reduction of electric conductivity resulting from fluid injection into the DFPS EAP-filled fracture would increase the surface-recorded electric field, as expected from Ohm's law. On the contrary, leakoff or compaction of the EAP-filled fracture would decrease the surface-recorded electric field.

Devine Fracture Pilot Site Layout

Fig. 2 shows a plan view of the DFPS wells crossing a previously placed horizontal hydraulic fracture, as described in detail by Ahmadian et al. (2018, 2019). A 4.5-inch internal diameter steel-cased well, perforated at 175 ft of depth, was used as the injection well. Devine Monitoring Wells (DMWs) 1 through 4 are located over a straight line at a relative distance of 10, 21.8, 45.8, and 80

ft away from the injection well. All DMWs are cased with schedule-40 PVC pipes with 2-inch internal diameter; DMWs 1 and 2 are screened from 170 to 180 ft of depth, and DMWs 3 and 4 are screened from 130 to 140 ft of depth. In addition, before this study, a new 5.5" ID PVC-cased well (DMW 9) was constructed at 107 ft from the injection well and screened at the fractured interval. DMWs 5 through 8 and the corner monitoring wells (labeled N, E, S, W) are not screened and were excluded from fluid pressure monitoring studies. However, the corner wells are instrumented with DAS fibers, which were used for estimating the time of arrival calculations. We used digital wellhead pressure transducers and downhole In-Situ™ pressure in the injection well, DMWs 1 through 4, and DMW 9, to record the wellhead pressure and BHP. In addition, a set of salinity monitor transducers, were deployed in these same wells to trace salinity during the operations (Fig. 2). Monitoring the bottomhole salinity and pressure at the screened intervals of DMWs 3 and 4 at a shallower depth than the fracture depth allowed to confirm the confinement of the injected fluids within the fracture zone. To keep the environmental noise to a minimum, the injection tanks and pumps were positioned 300 ft away from the injection well, and fluids were conveyed to the injection well using a 2-inch ID electrically nonconductive polypropylene pipe, which was laid on the ground surface.

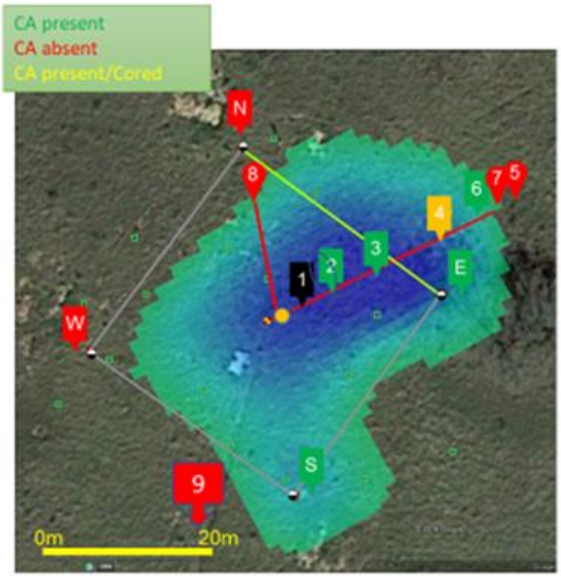

Fig. 2—Previously surveyed horizontal hydraulic fracture at the DFPS, adopted after Ahmadian et al. (2019). Green or red tags show the presence or absence of the contrast agent (CA) at a validation well location. Water injected into a previously placed and propped horizontal hydraulic fracture is shown by the green pea-shape area in the plan view, through a central injection well, the yellow circle.

Method

We employed Deep Imaging Technologies' (DIT) surface-based controlled-source EM (CSEM) equipment to evaluate the CSEM capability for real-time fluid tracking during injections at the DFPS. **Fig. 3** is a schematic depiction of this geophysical method. Two-orthogonal transmitter electrodes (depicted by the vertical yellow in Fig. 3), connected by a cable, are deployed on the surface. A set of sensitive receivers are distributed on the survey area (depicted by the yellow dots

in Fig. 3) on a cartesian grid and can register the X and Y component of the scattered field in both time and frequency domains. The x-axis is defined by the line connecting the injection well and DMWs 1-2. The transmitter line is parallel to the x-axis.

The measured electric fields (i.e., the scattered electric fields), which are the difference between the post-injection and pre-injection, are sensitive to the conductivity or resistivity change in the hydraulic-fracture zone. Therefore, by continuously measuring these field changes with time, the injected fluid movement in 3D could be inferred through EM forward modeling and inversion.

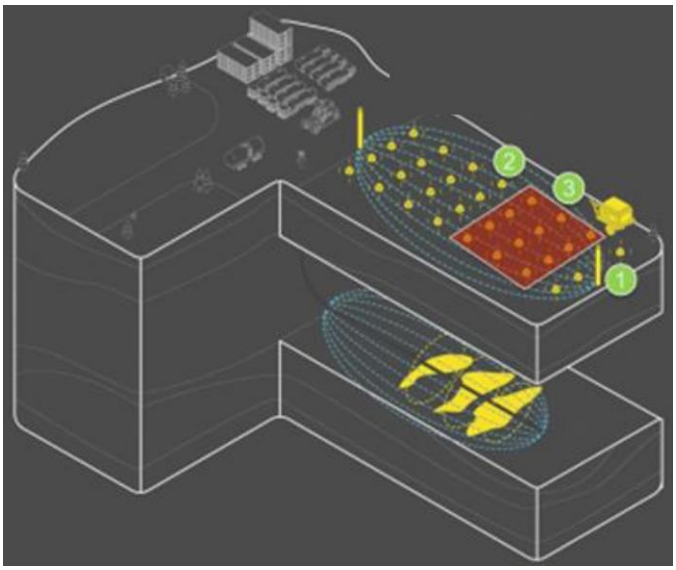

Fig. 3—A schematic diagram of a deep controlled-source electromagnetic (CSEM) imaging system used to image the injected fluid flow in real time. Surface transmitters far from the survey area transmit electric currents into the ground creating an electromagnetic (EM) field. Surface receivers, laid out in two lateral directions at the survey area, measure the electric potential difference before, during, and after injection, with 50,000 recordings per second. The receiver signals are processed for data quality. The scattered field at time *t* is obtained as the signal at time *t* subtracted by the baseline signal at *t*=0 (prior injection).

The layout of the surface receivers, transmitter line, the injection and monitoring wells, and the fracture boundary of the DFPS deployment are shown in **Fig. 4**. In this survey, we used 81 receivers in a cartesian pattern centered at the injection well and at 30 ft (9.14 m) of the distance between the receiver control units. In addition, we installed a transmitter line at almost 645 ft (197 m) of distance from the injection well. Each receiver in this survey area was associated with four 6-ft long copper electrode rods hammered into the ground to obtain the electric field on the ground surface in two lateral directions parallel to the alignment of the receivers in northeast-southwest and northwest-southeast directions. Two pairs of rods were associated with each receiver, installed in a lateral direction, and spaced by 25 ft (7.62 m).

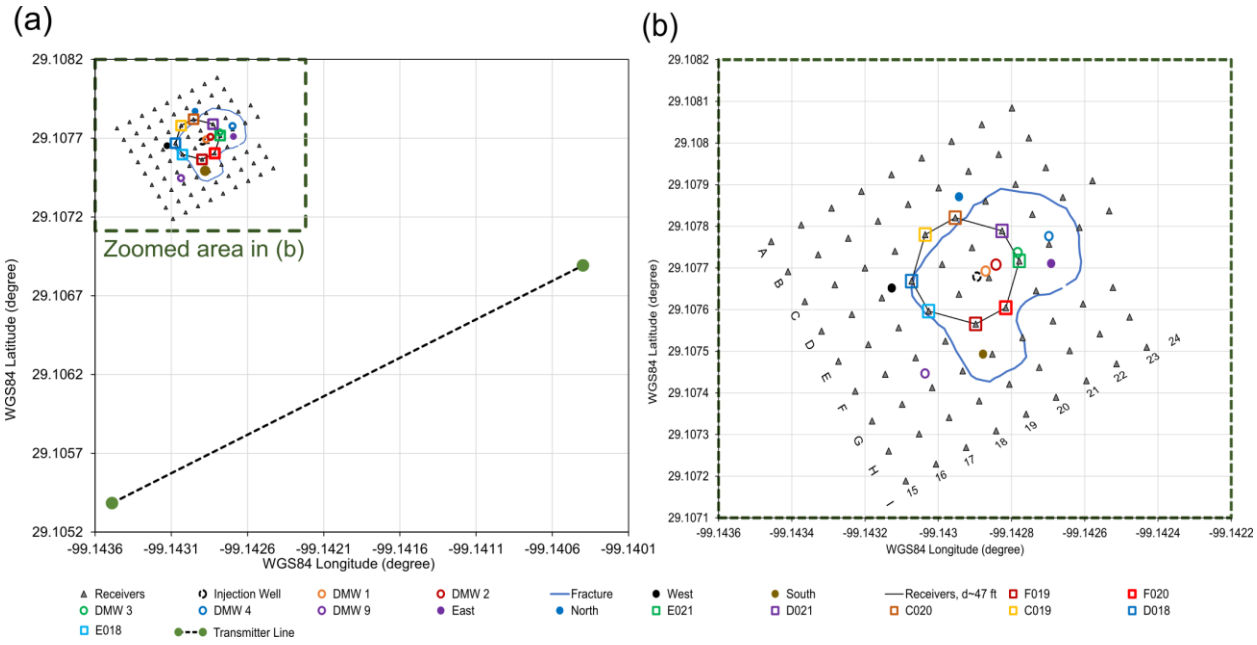

Fig. 4—CSEM Survey area in plan view at the DFPS in January 2022: (a) a zoom-out view including the transmitter line, receivers, wells, and the fracture shape; (b) a zoom-in view of the receivers, wells, and fracture boundary. The propped fracture boundary was derived from a previous survey during the primary hydraulic fracturing in 2017 (Ahmadian et al., 2019). Bottomhole pressure and salinity were recorded at the injection well and DMWs 1, 2, and 9 at 10, 20, and 107 ft of distance from the injection well. The receivers at 47 ft of distance from the injection well are highlighted as a reference for the electric potential-difference analyses below.

Oval-gear flowmeters manufactured by Macnaught Americas recorded the volumetric injection rate. To extend the range of flow rate measurement below 1 gallon per minute (GPM), we designed an injection manifold consisting of two flowmeters at low and high flow-rate ranges of 0.1-2.2 GPM and 2-18.5 GPM, respectively. In addition, we used two Precision Digital totalizers to log the flow rates through the injection time. Because of the sensitivity of the gears inside the flowmeters, we installed two strainers at the inputs of the flowmeters to remove debris in the injection water before entering the flowmeters. Furthermore, we installed two ball valves at the inlets of these flowmeters to control the flow direction through these flowmeters. Generally, at the start of injection, due to the small flow rates, we opened flow through the low-flow-rate meter, and at a later time, when the flow rate increased, we switched the main flow line toward the high-flow-rate meter. The digital, wireless pressure transducers before and after this manifold informed us about the pump outlet pressure and any pressure-drop anomalies through this manifold.

We conducted ten injection cycles at the DFPS, as listed in **Table 1**, simultaneous with surface CSEM surveys, tiltmeter mapping, and fiber-optic monitoring. During this deployment, we also tested a new generation of electromagnetic wireless receivers that allowed for real-time communication with a command center deployed to the DFPS. However, we experienced a few equipment failures on multiple receivers during the initial injection cycle on January 21. In subsequent trials, we were able to collect data for all the planned injection scenarios. For brevity of the current manuscript, we will focus only on the first four survey days and defer discussions about the remaining survey days to our future work. These four survey days are listed in the following:

1. On January 23, we injected freshwater to test EM response due to variable flow rates;
2. On January 24, we injected freshwater at higher rates compared to the rate on January 23;
3. The January 26 injection was a repeat of the injection on January 24;
4. On January 27, we repeated the January 26 injection with the change of the injected fluid from freshwater to saltwater; and

Due to an operator error, which led to the introduction of a pressure spike at the beginning of the January 24 injection, this experiment was repeated on January 26, and the dataset for January 24 is excluded in the following discussions. It is essential to note that the observations recorded by all instruments may be influenced to some extent by the cumulative injection volumes and leakoff before each cycle. Therefore, most data interpretations from geophysical equipment were conducted by subtracting recorded values from an initial starting value each day.

Table 1—Summary of five injection cycles during the injection campaign in January 2022 at the DFPS. Injections before 1/27 included only injection of freshwater at different volumes. The injections on 1/27 included freshwater and saltwater slugs. A surface-line and injection-well refilling interval precede each injection cycle before pressuring the formation. Throughout this report, we used military time style for reporting daily time, starting from 00:00 at midnight, moving to 12:00 at noon, and finishing the daily time at 23:59.

Injection Cycle No.	Date (day/month/year)	Injection Scenario	Injection Slug	Refilling start time (hour: minute)	Refilling finish time (hour: minute)	Shut-in time (hour: minute)	Injected Volume (US Gallons)
1	1/21/2022	Repeating 9/20/2020	Freshwater	9:28	10:48	15:14	1126.02
2	1/23/2022	Flow-rate Test	Freshwater	11:31	11:41	16:50	603.38
3	1/24/2022	Freshwater Injection	Freshwater	12:00		16:35	952.1
4	1/26/2022	Freshwater+Chase Freshwater Injection	Freshwater	12:00	12:03	17:56	1200.2 (freshwater)
5	1/27/2022	Saltwater+Chase Freshwater Injection	Small Saltwater Slug+Large Freshwater Slug	12:00	12:06	18:06	215.6 (saltwater); 990 (freshwater)

The bottomhole pressure (BHP) for the injection well, DMWs 1-4, and DMW 9, the ambient pressure, and the flow rate during the January 21-27 injection cycles are shown in **Fig. 5**. The BHP changes during all injection cycles agree with event logs and digital wellhead pressure transducers.

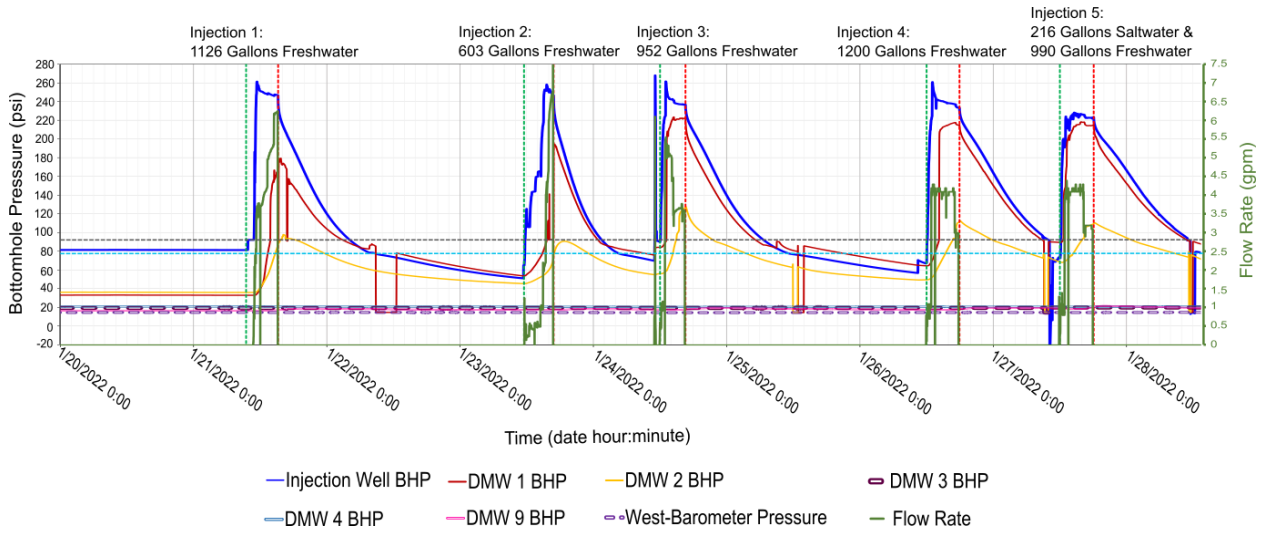

Fig. 5—Bottomhole pressure for the injection well and DMWs 1-4 and 9, ambient pressure, and flow rate during the January 21-27 injection cycles. The horizontal black dashed line = the hydrostatic pressure of 92.15 psi for a 175-ft long water column in the injection well plus the atmospheric pressure. The horizontal blue dashed line = the hydrostatic pressure of 77.33 psi for a 175-ft long water column in the injection well. The bottomhole pressure drop below 77.33 psi during shut-in shows the development of vacuum pressure in the corresponding well.

Results

Surface Recorded Electric Potential Difference

Our initial analysis relied on the movies that the DIT had supplied us, which compared the change of electric field with respect to a reference starting time, t_0. **Table 2** shows an exemplary set of movie clips for the evolution of the electric field on January 26, along with additional coinciding recorded events: flow rate, cumulative injected volume, and pressure. Having plotted these electric potential differences for the x- and y-component of the electric field, the DIT suggested that the diurnal effects are coupled with the x-component of the electric field due to the large swings in the daily temperature, after 22:00 on January 26 injection cycle. However, the Y-component of the electric field was decoupled from these diurnal effects. Thus, to unify the interpretation of the results, we decided to limit the initial interpretation to the magnitude of change in y-axis electric field magnitude only, defined as the absolute of the total y-axis field amplitude at a specific time subtracted from the total y-axis field amplitude at t_0, as **Eq. 1**:

$$\text{Magnitude of change in y-axis electric field magnitude} = ||E_y(t)|-|E_y(0)||, \quad (1)$$

where $E_y(0)$ and $E_y(t)$ denote the y-axis electric field complex vectors (composed of real and imaginary parts, $\text{Re}(E_y)$ and $\text{Im}(E_y)$) at time 0 and time t, respectively. Time 0 was selected arbitrarily, commonly chosen a few minutes before the start of injection. This calculation only reflects the magnitude of this subtraction rather than its sign. However, calculating this change without the internal absolute signs also returned very close values. The second row in Table 2 represents the snapshots of the parameter in Eq. 1 at various times. In addition, phase-amplitude was computed by **Eq. 2**:

Phase change in y-axis electric field $= tan^{-1}(Im(E_y(t))/Re(E_y(t))) - tan^{-1}(Im(E_y(0))/Re(E_y(0)))$. (2)

A large expansion of the color contours occurs for the phase change (the third row in Table 2), showing the most considerable sensitivity of this parameter to injection at early times.

Table 2—Evolution of the change in y-axis electric field magnitude and scattered E_y field phase at the beginning of injection, from 11:55 until 12:15 on January 26. The events, flow rate, cumulative injected volume, and BHP are listed through time. The change in electric field magnitude is normalized for 1 ampere of electric current following industry convention. For the actual electric current of 20 amperes, these amplitudes should be multiplied by 20. The color contours for all these parameters start to grow from the central injection well. During this early time, the largest change of the snapshots occurs during the surface line refilling, which is likely related to the release of the trapped water inside the injection well into the proppant pack once the wellhead valve was opened at the beginning of the refilling.

Time	11:55	12:00	12:05	12:10	12:15	Legend
The magnitude of change in y-axis electric field magnitude	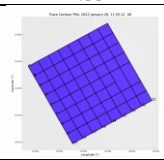	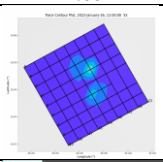	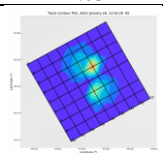	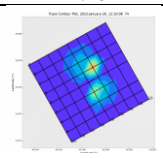	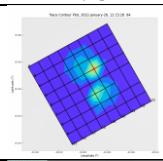	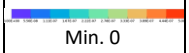 Min. 0 Max. 5e-7 (V/m)
Y-Axis phase change	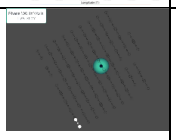	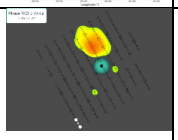	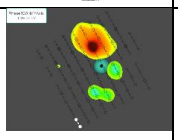	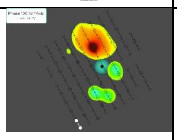	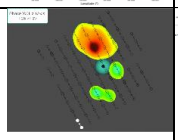	 Min./Max. -+2e-2 Noise Floor -+2e-3
Event	-	Started refilling	Started injection	-	-	
Injection flow rate (gpm)	0	0	0.6	0.6	0.5	
Cumulative volume (gal)	Cumulative injection so far: 2713	0	0.6	2.9	5.1	
BHP (psi)	67	67.4	92	98	124.7	

Because showing hundreds of movie clips in this paper is not practical, we devised a simplified routine to report the data. This routine is based on plotting the individual receiver scattered electric potential difference combined with the flow rate and BHP through time. To calculate the scattered electric potential difference, we multiple Eq. 1 by the distance (7.62 m) between the surface electrodes. Also, to ensure that a unified method is used to compare the electric potential differences, we only plotted the signal from the receivers at a 47 ft distance from the injection well. We also conducted this analysis for receivers at nearer or farther distances from the injection well. The general conclusion was that the electric potential difference reduced as the distance to the injection well increased (data not shown).

Figs. 6 through **8** plot the electric potential difference from the magnitude of change in Y-axis electric field magnitude for a group of individual receivers at a constant distance of 47 ft from the injection well for January 23 (Fig. 6), January 26 (Fig. 7), and January 27 (Fig. 8). To assess the relationship between the electric field changes and flow rate or BHP, we combined these plots with the injection flow rate and BHPs at the injection well, DMW 1, and DMW 2. This combination of plots helped us to quickly compare the governing parameters of the fracture

behavior with the electric potential-difference changes. In Fig. 6, three important intervals can be observed in the electric potential differences, as elaborated in the following:

Interval 1 spanned the time interval when the surface line and injection wellbore were refilled with freshwater after opening the injection wellhead valve, coinciding with an abrupt increase in the electric potential difference. As stated above, we believe this sharp increase in the electric potential difference is because of releasing the trapped water in the injection well into the formation by opening the wellhead valve. As suggested by the lab studies (Fig. 1), the rush of water into the EAP layer could change the conductivity of the EAP-filled fracture. Even during the continuous overnight leakoff associated with the previous injection cycle, the water in the wellbore was trapped inside the injection well because the wellhead valve was tightly closed during this leakoff. This is analogous to the trapped water in a straw placed in a cup of water, while one holds their thumb on the straw's opening; when the thumb is removed, the water trapped in the straw rushes into the cup. We observed a similar early-time jump of the electric potential difference during refilling on January 26 (Fig. 7). However, we did not observe this behavior on January 27 (Fig. 8). This is because the injection cycles before January 27 had loaded the formation with 3912 US gallons of water. This slowed down the injected water leakoff into the formation on January 27, leading to negligible wellbore water flow into the formation after opening the injection wellhead valve. These phenomena correspond to the BHPs that fell below the hydrostatic pressure of 77.33 psi at the injection well, DMW 1, and DMW 2 during shut-in on January 23 through 26, and in contrast, remained above 77.33 psi on January 27 (see the dashed blue horizonal line on Fig. 5). Because the host rock was at a lower pressure on earlier days due to fewer pre-injected volumes, this likely led to significant vacuum pressures on January 23 and 26 compared to no vacuum pressure on January 27.

The trapped water volume inside the 175-ft-long injection well amounts to about 145 gallons. Assuming that this amount of water rushes within seconds of opening the wellhead valve into the formation at vacuum pressure, the flow rate at the start will likely be much higher than any flow rate we achieved during the controlled experiments. Even if we assume that the release time of this volume into the formation was 10 minutes, the resultant flow rate would be almost 15 gpm, nearly twice the highest recorded flow rate during the injection cycles. As elaborated in the following section, if flow rate changes are high, the streaming potential (SP) could become a significant contributor to the observed electric potential changes at any interval.

Interval 2 in Fig. 6 spans the time interval of injection at low flow rates (equal to or below 1 gpm), also characterized by the gradual decline of the electric potential difference. The flow rates smaller than 0.5 gpm throughout this interval were likely inadequate to provide enough fluid volume to reopen the fracture. Aside from the SP effect, another possible explanation for this slow decline in electric field observed can be attributed to the gradual rearrangement of the EAPs back to a more compacted form with respect to the disturbed state in Interval 1. As shown previously, when the EAPs are packed, the electric conductivity increases. As a result, the electric field signal may decline.

Interval 3 in Fig. 6 represents the exceedance of the injection flow rate above 1 gpm. The observed rise in the electric potential in this period follows this jump in flow rate, as well as a jump

in the BHP. At the beginning of this interval, the injection-well BHP exceeds the fracture closure pressure (FCP) of 154 psi (Haddad and Ahmadian, 2023), leading to the fracture reopening near the injection well. Consequently, we observe the change in the trends of the electric potential difference of all receivers from declining to plateau at the beginning of Interval 3. These trends were followed by a significant increase in the electric potential difference. This is likely due to the increased separation and resistivity of the EAP grains during further extension of the reopened fracture area.

We observed the same signal trends in the electric potential differences for the receivers at other distances from the injection well. However, compared to the electric potentials in Fig. 6, all electric potential differences at a larger distance from the injection well rise to smaller peaks, showing the effect of distance from the injection well on the surface electric potential difference (for brevity, the data are not shown). The unequal magnitude of electric potential difference (also clearly seen in the first row of Table 2) at equidistant receivers suggests an asymmetric fluid flow away from the injector well, showing the ability of the surface CSEM to detect the predominant fluid flow direction in the EAP-filled fracture at the DFPS. To avoid busy plots, in subsequent Figs. 7 and 8, we only show the temporal change in the measured electrical potential for a single receiver (F019), with the maximum magnitude among eight equidistant receivers.

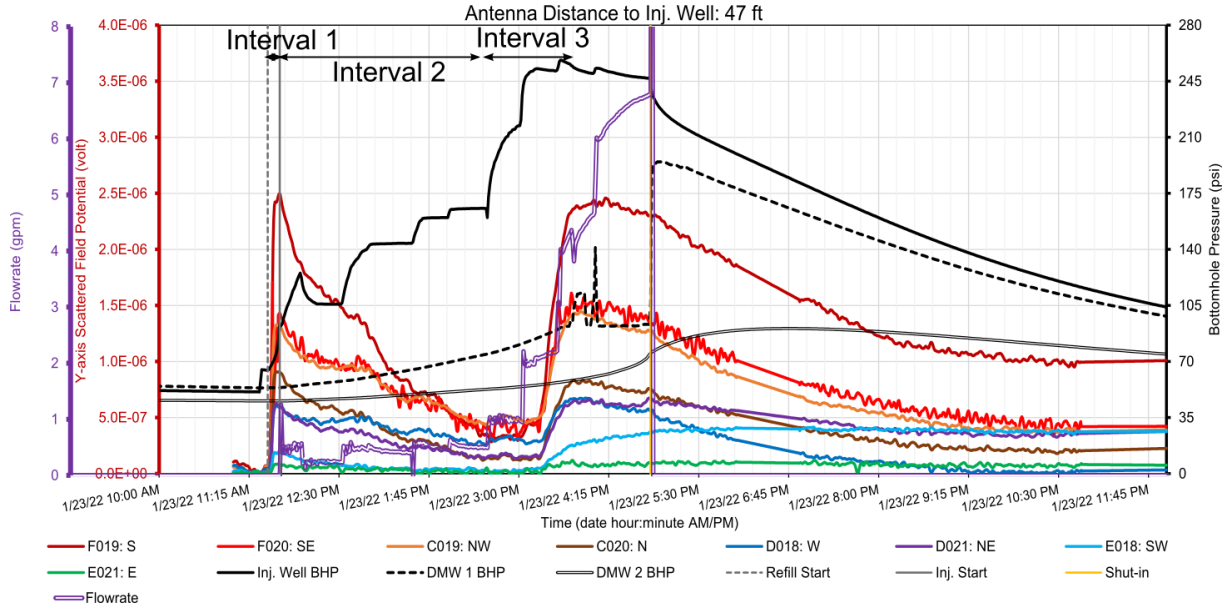

Fig. 6— January 23 injection results. Temporal change of the scattered field in receivers at 47 ft of distance from the injection well, flow rate, and the BHP at the injection well, DMW 1 and DMW 2. The receiver locations are shown in Fig. 4b. The vertical black lines indicate the starting and finishing times of refilling the surface line and the injection well with water during Interval 1.

The January 26 injection was analogous to the injection experiments we had conducted during a previous injection campaign in September 2020 (Haddad et al., 2021, 2023). It involved injecting almost 1200 gallons of freshwater in six hours. Fig. 7 shows the electric potential difference associated with receiver F019, combined with the flow-rate profile and BHPs for the injection well, DMW 1, and DMW 2. Similar to January 23 (Fig. 6), three remarkable intervals can be

identified in the electric potential difference: Interval 1, concurrent with the sudden flow of the trapped water inside the injection well into the EAP pack; Interval 2, coincident with the gradual drop of the signal, presumably due to the EAP resettlement; and Interval 3, concurrent with the signal increase due to the sharp increase of the flow rate and significant fracture reopening. Because increasing the flow rate to 4 gpm during Intervals 1 and 2 took almost four hours on January 23 and only one hour on January 26, the change of the electric field trend from a declining to inclining during Interval 2 to Interval 3 on January 26 was much more rapid than January 23. This suggests that the resident EAP pack is sensitive to in-situ flow-rate changes. We notice a 20-minute delay in registering an increase in the electric field once the flow rate exceeds 1 gpm in Interval 3.

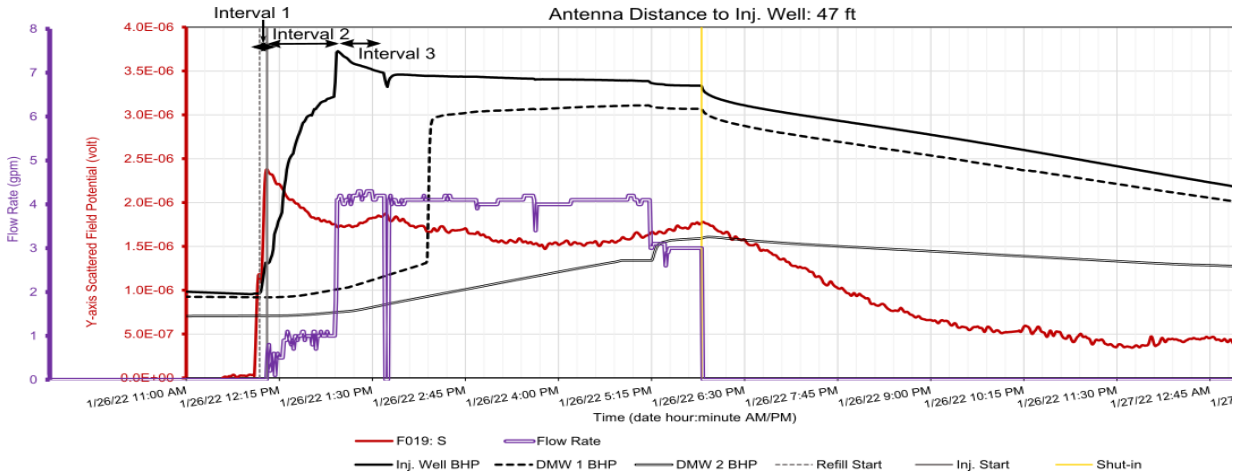

Fig. 7— January 26 injection results. Temporal change of the scattered field at receiver F019 at a distance of 47 ft from the injection well, flow rate, and the BHP at the injection well, DMW 1 and DMW 2. Interval 1 corresponds to the surface-line refilling period, and Intervals 2 and 3 correspond to the declining and inclining trends of the electric potential differences. A solid yellow vertical line represents the start of the shut-in period when EAP compaction dominates and electric potential differences drop. The receiver location is shown in Fig. 4b.

Fig. 8 shows the electric potential difference at the F019 receiver for the January 27 injection. Again, this plot combines the flow-rate profile, BHP, and bottomhole salinity at the injection well, DMW 1 and DMW 2. The injection cycle started by refilling the surface line and the injection well at noon, followed by pressurizing the injected fluid at 12:08 (Interval 1 in Fig. 8). Two slugs were injected during this cycle. The first injection slug was 200 gallons of saltwater at 2500 ppm, followed by the injection of a freshwater slug of 990 gallons. Considering that there were approximately 200 gallons of freshwater on the surface line and the injection well cumulatively before we started injection on this day, it took 1 hour and 15 minutes (until ~13:25) for the saltwater slug to arrive at the injection well perforations. One similarity between the shown parameters in Figs. 6, 7, and 8 for January 23, 26, and 27 is that the abrupt increase of the flow rate to 4 gpm is followed by a second peak in the electric potential difference, marked by the end of Interval 3. Comparing the electric field trends in Figs. 6, 7, and 8 for January 23, 26, and 27 reveals the following differences:

1. an absence of an inclining trend during Interval 1 on January 27;

2. the presence of only a declining trend during Interval 2 (when the flow rate is below one gpm) on January 23 and 26 (Figs. 6, 7), versus the presence of *both* inclining (Interval 2a) and declining (Interval 2b) trends on January 27, before the increase of the flow rate to 4 gpm (Interval 3); and
3. a longer delay on January 27 injection to reach the second incline in potential difference trend after the injection-well BHP exceeded the FCP (60 minutes, 40 minutes, and no delay for 1/27, 1/26, and 1/23, respectively). This difference infers that more injected volumes may be needed during subsequent injections to change the electric potential trend from declining to inclining. This is supported by the increase of the initial BHP at each subsequent cycle during our study.

Some of these differences could be attributed to the different extent of the invaded formation and fracture zones by the previously injected volumes as the injection cycles proceeded. The injected volume was 3900 gallons at the beginning of the January 27 injection cycle, and it was only 2700 gallons at the beginning of the January 26 injection cycle. In addition, there was an additional leakoff day before the start of the January 26 injection. During Interval 2 on the January 27 injection, we noticed that the BHP only rose to 220 psi versus 260 psi for the January 26 injection. After the initial rise to about 200 psi, the BHP flattened during Interval 2a for about 30 minutes on January 27. This may indicate that a new channel may have formed during the January 27 injection.

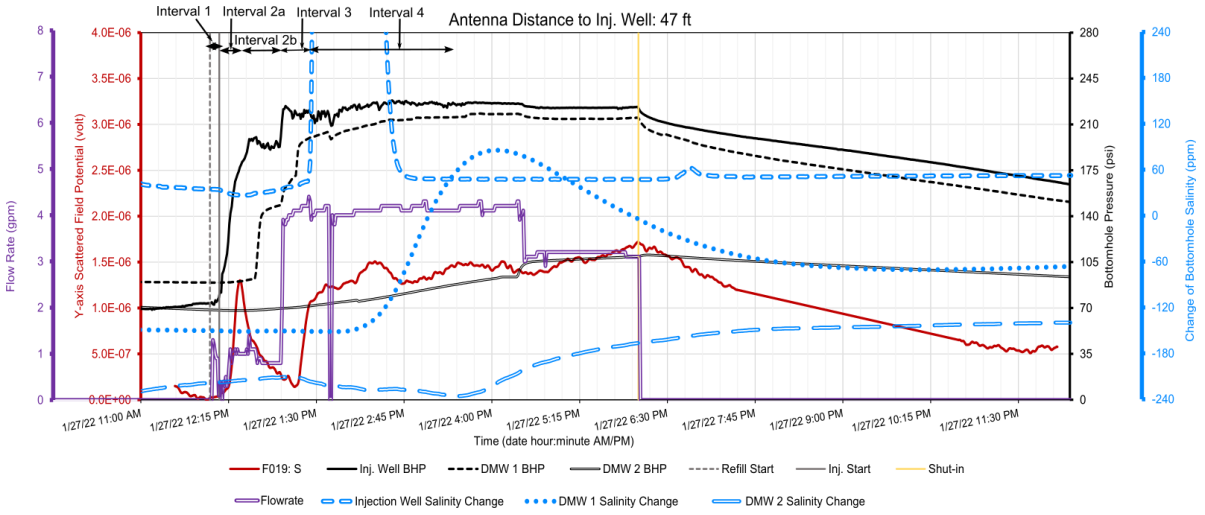

Fig. 8— January 27 injection results. Temporal change of the scattered field at receiver F019 at 47 ft of distance from the injection well, flow rate, salinity, and the BHP at the injection well, DMW 1 and DMW 2. The receiver location is shown in Fig. 4b. The vertical black lines indicate the starting and finishing times of refilling the surface line and the injection well with water during Interval 1. The solid yellow vertical line represents the start of the shut-in period when EAP compaction dominates, and electric potential differences drop. Salinity increased at the injection well, DMW 1 and DMW 2 at 13:25, 14:15, and 15:35, respectively. Salinity in the injection well reached 2500 ppm, clipped to zoom into the salinity ranges for the other wells more clearly. Intervals 2a and 2b contain inclining and declining trends that were not observed in the previous days. Interval 3 corresponds to the electric potential differences' major inclining trend related to the flow-rate increase to 4 gpm. Interval 4 corresponds to the period at 4 gpm before the salinity slug reached DMW 2.

The only major difference between injections on January 26 and 27 was the salinity increase to 2500 ppm for the initial 200 gallons of injection on January 27. In contrast, only freshwater was injected on January 26. However, the electric field drop in Interval 2b on January 27 cannot be attributed to salinity. This is because we observed the decrease in the electric field in Interval 2 before saltwater had entered the formation. Moreover, even though the abrupt increase of the electric potential difference at 13:22 coincided with the rise of downhole salinity inside the injection well (Fig. 8), because the salinity arrives at the injection perforation at roughly 13:25, it seems unlikely that increase of potential difference during Interval 3 is due to salinity changes. On the other hand, it appears that gradual fracture dilation and area extension, as a result of an abrupt flow-rate change at 13:00, dominates any possible effects of up to 200 gallons of 2500 ppm salinity changes during interval 3. The 20-minute delay in the rise of the electric field potential, after the flow-rate increase beyond 1 gpm, was also observed during the other days.

The first peak of the electric potential differences on January 27 coincides with the exceedance of the injection-well BHP from FCP (end of Interval 2a in Fig. 8) and a flow rate change. Therefore, we can attribute this peak to 1) the temporary fracture reopening and the reduction of the proppant pack conductivity due to freshwater injection, followed by fracture closure due to too low injection flow rate to keep the fracture open, and 2) streaming potential due to flow rate changes. In all injection cycles, after shut-in, the fluid leakoff and the EAP-pack compaction increased the electric conductivity and may have contributed to the observed decrease in the electric field.

A possible saltwater effect can be observed after Interval 3 during multiple smaller peaks and troughs in electric field traces on January 27 (Fig. 8). The peaks seem to correspond to the salinity peaks at the injection well, DMW 1, and DMW 2 (Fig. 8). Together, these results suggest that fracture dilation, compaction, and flow-rate changes play a dominant role in the variations of the observed electric field on January 27.

Total and Scattered Field Magnitudes

To better explain possible causative mechanisms for the measured electric field data, we conducted simple quantitative analyses to compare signal amplitude for the scattered electric field using analytical solutions to calculate the SP and conventional EM modeling results.

The synthetic EM data was generated by the Discontinuous Galerkin Frequency-Domain (DGFD) method (Fang et al., 2020; Zhang et al., 2020, 2022; Sun et al., 2021). The simulation model is based on the configuration of the January 2022 experiment at the DFPS (Fig. 4). **Fig. 9a** shows a cross-sectional view of our multilayered model, showing the assumed conductivity values for all layers, which were obtained by running induction well logs at the DFPS in 2018 (Ahmadian et al., 2019). The center of the coordinate system is at the injection well, the x-direction is the line from the injection well toward DMWs 1-4, and the z-direction is the opposite direction of depth. This coordinate system follows the right-hand rule, meaning that the y-axis points toward the northwest, as the x-axis (the axis going through DMWs 1-4) is toward the northeast. To match the field results better, the surface layer of the model was divided into multiple zones according to the measured surface conductivity values at the DFPS. In those studies, a dense surface conductivity

survey was conducted through an 8×10 grid over the fracture boundaries, using a CMD-Explorer electromagnetic conductivity meter. The resulting values are shown in **Table 3** and by the dark-gray zone in **Fig. 9b**. We also measured conductivities beyond this zone using a conventional Schlumberger array, as shown in Fig. 10b.

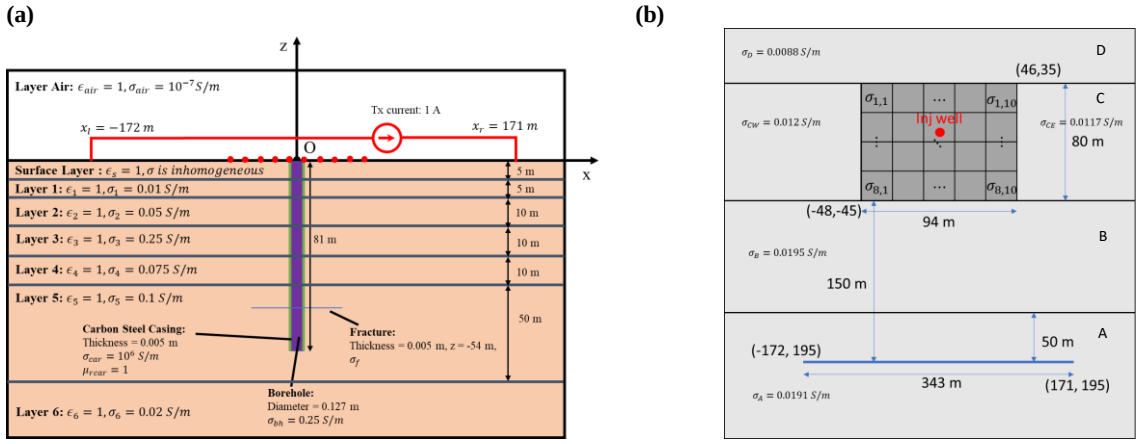

Fig. 9—(a) The x-z cross section of the DGFD layered model including seven layers in the model with embedded permittivity and conductivity values. Fracture is assumed to be a thin sheet with an initial conductivity value of 60 S/m. (b) Plan view of the model, including the schematics of an inhomogeneous surface layer shown by dark-gray meshed area overlying the propped fracture and where receivers are installed. All layers were assumed to be homogeneous except for the surface layer. The red TX line in (a) = the transmitter. The red RX dots in (a) = a line of receivers. The surface layer in (b) is divided into areas A through D from south to north. Area A, B, and D conductivities are marked in (b). Area C conductivity surveyed by a CMD-Explorer electromagnetic conductivity meter (GF Instruments, S.R.O.), and gridblock calculated by averaging the CMD-Explorer measurements within each gridblock of an 8×10 mesh.

Table 3—$\sigma_{i,j}$ conductivity in mS/m for each gridblock within the dark-gray area in Fig. 9. The indices 1 through 10 on the first row = the gridblock number from left to right in Fig. 9. The indices 1 through 8 on the first column = the gridblock number from top to bottom in Fig. 9.

		x-index									
		1	**2**	**3**	**4**	**5**	**6**	**7**	**8**	**9**	**10**
y-index	**1**	9.9	10	11	5	5	10	10	13.8	10	13.8
	2	9	12.5	5	11	8	10.6	20	9.9	13.8	13.8
	3	13.8	10	15	20	7	9	20	11.9	30	30
	4	5	12.5	10	10	10	30	11.8	9.6	10	20
	5	20	12.5	20	20	0.4	10	9	9.6	10	11.9
	6	13	0.2	20	20	20	8	8	9.6	5	11.9
	7	5	15	0.4	12.5	30	5	5	9	9	9.6
	8	14	10	12.5	12.5	10	10	9.5	9.5	9.5	9.6

We compared the forward modeled total electric field to the measured values just before the water injection on January 26 (**Fig. 10**). We defined the mismatch between these contours as the average of the difference between the amplitude of the total electric field obtained from the simulation and the field data in 81 discrete data points at receivers. This average mismatch was 29%.

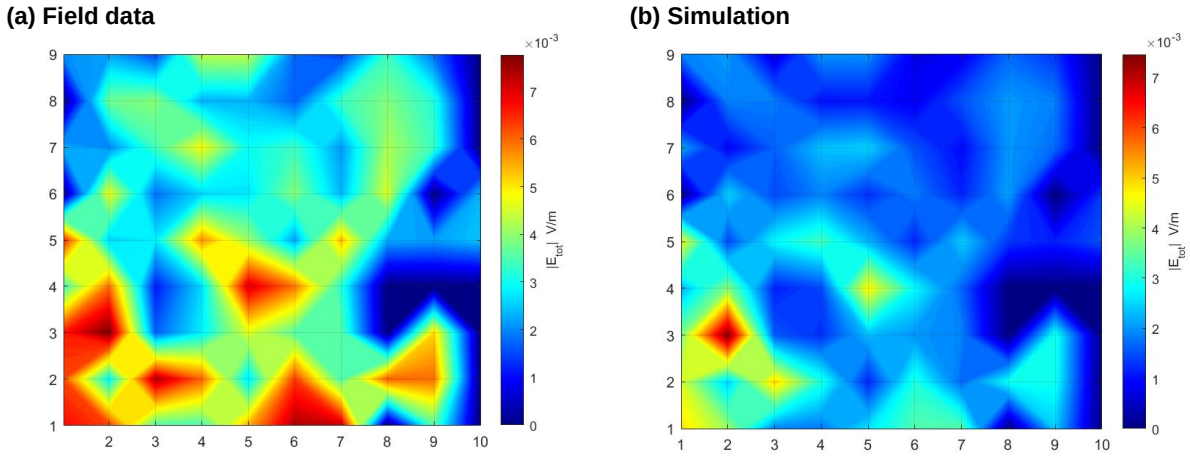

Fig. 10—Total electric field in the plan view, on January 26 at 10:00 am, obtained from (a) the field data and (b) simulation.

Next, we considered three states of the dilated fracture on January 26, 2022, to simulate the deviation from the total field due to conductivity changes (**Table 4**). We labeled these as:

- State 1, at 12:18, with a change of the electrical conductivity from the background 60 S/m to 40 S/m in a circular area of the propped fracture, around the injection well, with a radius of 1.34 m;
- State 2, at 17:33, with a change of the electrical conductivity from the background 60 S/m to 10 S/m in a circular area of the propped fracture, around the injection well, with a radius of 4.6 m; and
- State 3, at 22:26, with a change of the electrical conductivity from the background 60 S/m to 40 S/m in a circular area of the propped fracture, around the injection well, with a radius of 3 m.

States 1 and 2 correspond to 12 minutes and approximately 5.5 hours after the start of injection, respectively. States 2 corresponds to 4.5 hours after shut-in. The background conductivity of 60 S/m was obtained from the conductance of 300 mS, from our previous induction logs at DFPS, divided by 0.5 cm thick propped fracture (Ahmadian et al., 2019). The 40 S/m conductivity in State 1 was estimated because FCP was not exceeded. However, we assumed that further injection until State 2 led to the drop of conductivity in the circular area down to 10 S/m due to further dilation of the fracture. Our lab observations support these assumed trends (see Fig. 1). At State 3, we assumed that leakoff led to the increase of conductivity, back to that of State 1. The dilated fracture dimensions were determined using the cumulative injected volume at each point and the conservation of mass. The scattered field was calculated by subtracting the total field at the initial time before the start of injection from the total field at a specific state.

As shown in Table 4, the mismatches of the simulated scattered electric field amplitude from the field data are 228%, 59%, and 83% for States 1, 2, and 3, respectively. These mismatches were calculated from the difference between the scattered field amplitude obtained from the simulations and field data at individual receivers as plotted in **Fig. 11**, according to **Eq. 3**:

$$\text{Mismatch}(|E_f^{sct}|, |E_s^{sct}|) = \sqrt{\sum_{i=1}^{N}\left[\left(|E_{f,i}^{sct}| - |E_{s,i}^{sct}|\right)^2\right]} \Big/ \sqrt{\sum_{i=1}^{N}\left[|E_{s,i}^{sct}|^2\right]}, \quad (3)$$

where $|E_{f,i}^{sct}|$ and $|E_{s,i}^{sct}|$ are the scattered field amplitude from the field data and simulation at receiver *i*, and *N* denotes the number of receivers, which is 81 in this work.

The maximum mismatch at State 1 shows that the EM model fails to simulate conductivity changes at early time and yet may be more suitable for the simulation of conductivity changes at later stages of injection and leakoff. This reveals that the conductivity changes that induced the EM field by themselves cannot justify the large potential differences observed on the ground surface at the early time. Instead, this large gap can likely be explained by SP.

Table 4—Three states of the dilated fracture on January 26, 2022, for the calculation of the scattered field. The mismatch column refers to the difference in the scattered field amplitude obtained from the simulation and the field data. The mismatch is obtained from averaging the actual difference between the simulation and field data for all receivers (Fig. 11).

State	Time	From Simulation		From Field Data		Mismatch (Average of all receivers)
		Scattered Field Amplitude Maximum (V/m)	20× Scattered Field Amplitude Maximum (V/m)	Scattered Field Amplitude Maximum (V/m)	20× Scattered Field Amplitude Maximum (V/m)	
S_1, 1.3 m, 40 S/m	12:18	1.2×10^{-7}	2.4×10^{-6}	4.8×10^{-7}	9.6×10^{-6}	228%
S_2, 7.65 m, 10 S/m	17:33	3.4×10^{-7}	6.8×10^{-6}	3.4×10^{-7}	6.8×10^{-6}	59%
S_3, 3.0 m, 40 S/m	22:26	1.2×10^{-7}	2.4×10^{-6}	1.4×10^{-7}	2.8×10^{-6}	83%

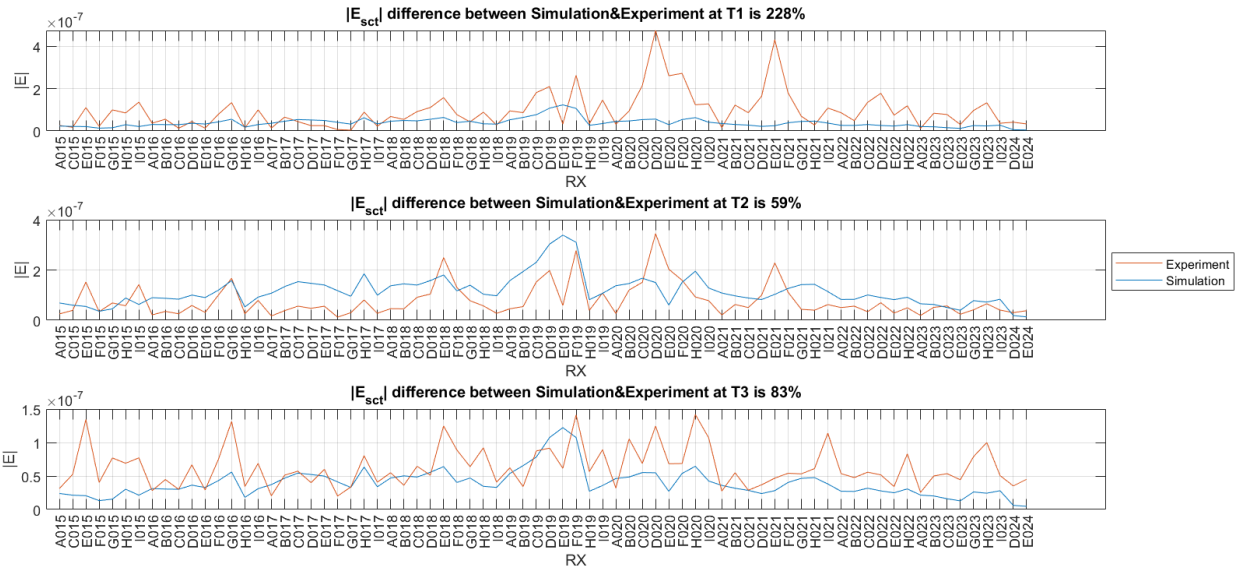

Fig. 11—Comparison of the scattered field amplitude (|E(t)-E(0)|) from the EM simulations (blue line) and field data (orange line) at all receivers, at specific times: (upper) S_1 or 12:18; (middle) S_2 or 17:33; (lower) S_3 or 22:26.

Streaming Potential Theory and Analytical Solution

In the SP theory, large spatiotemporal fluid pressure changes and fluid injections into a medium can induce detectable electric currents (De Groot & Tolhoek, 1951; Fitterman, 1979; Sill, 1983;

Ishido et al., 1983). With access to the gradient of the hydraulic head, the SP, or ϕ, can be obtained by solving the following Poisson's equation (**Eq. 4**):

$$\nabla.\sigma\nabla\phi=-\nabla.L\nabla h, \quad (4)$$

where σ and L denote the electrical conductivity and cross-coupling coefficient, respectively. The hydraulic head gradient can be obtained by solving the diffusivity equation (**Eq. 5**):

$$\nabla.K\nabla h= S_s\frac{\partial h}{\partial t}-Q_h, \quad (5)$$

where K denotes the formation permeability, S_s represents specific storage, and Q_h is the injection rate. The temporal flow-rate profile is the input to Eq. 5, and ∇h is retrieved from this equation to be used in Eq. 4 to calculate the SP. The poroelastic models developed by Haddad and Ahmadian (2023) can solve Eq. 5 fully coupled with stress equilibrium equations. Evaluating the SP induced by changes in the hydraulic head needs postprocessing of pore-fluid pressure distribution obtained from this poroelastic model at each time increment to calculate the spatial changes in the hydraulic head. This poroelastic model can determine the spatiotemporal pore pressure gradient as a function of the dilated fracture area, rock deformation, fluid leakoff, and gap flow through the proppant pack (Haddad and Ahmadian, 2023).

Fig. 12 shows the comparison of the total electric field amplitude from the field data and simulation with the estimated SP electric field using an analytical solution (Sheffer and Oldenburg, 2007), with corresponding values for State 1. To generate the SP solution, we assumed a steady-state flow and a uniform half-space model. The injection rate, Q, hydraulic conductivity, K, the cross-coupling coefficient, L, and the conductivity of the uniform half-space, σ, the injection source depth, h, and the source volume, v_s, are listed in Fig. 12c. We assumed v_s as unit volume. The computed SP electric field amplitude rises to a maximum of 8.5×10^{-6} V/m. Despite the convention of reporting scattered field amplitude per unit electric current, we normalized the scattered field amplitudes at a current of 20 Amp, which is the current applied during the CSEM survey at the DFPS. This multiplication was essential to make the active-source scattered electric field comparable to a passive-source SP. As shown in Fig. 12, the maximum scattered field amplitude from the field data at State 1 was 9.5×10^{-6} V/m, and was computed to be only 2.4×10^{-6} V/m from the EM simulation. However, the maximum SP electric field amplitude is 8.5×10^{-6} V/m. This comparison reveals a quite significant phenomenon: SP may dominate the observed field responses a State 1 of the January 26 injection.

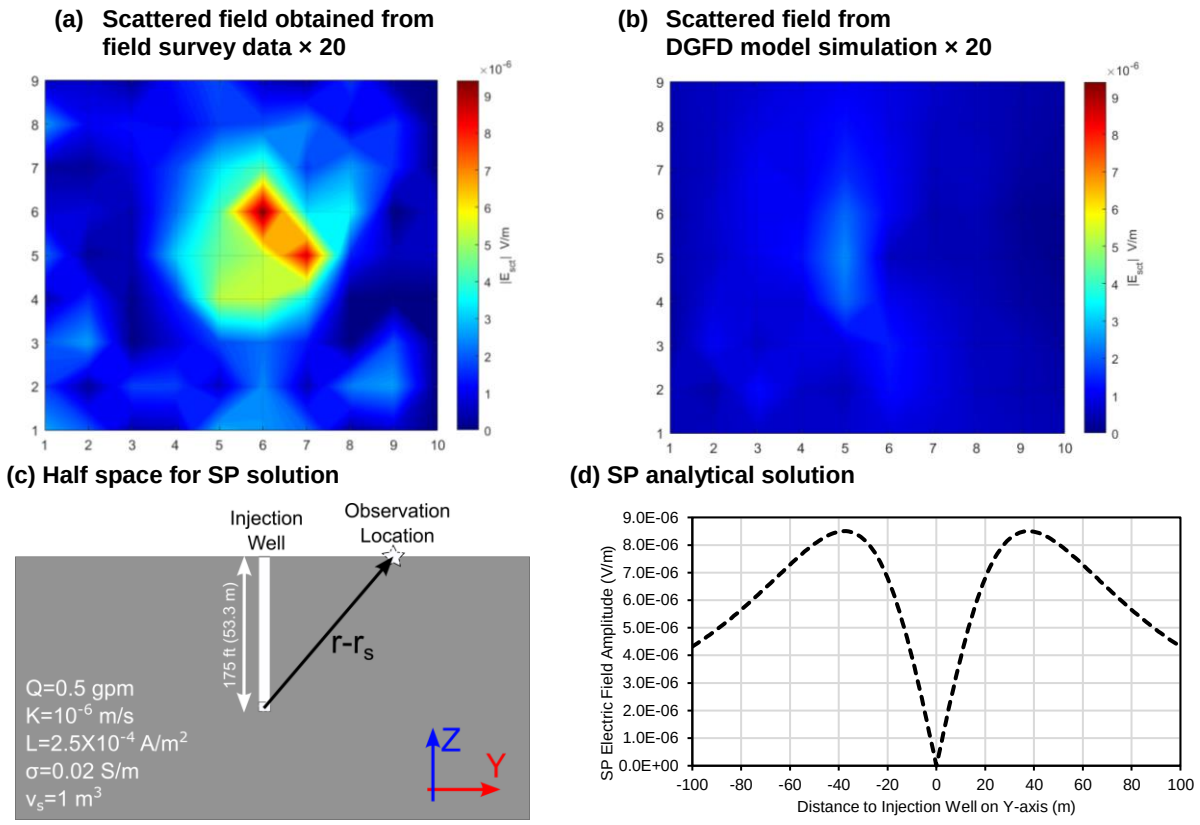

Fig. 12—(a) Scattered field magnitude from the field data. (b) Scattered field magnitude from the DGFD simulation. (c) Cross section of a half-space, homogeneous model to calculate the SP due to injection into the media through a single-point perforation at a depth of 53.3 m (175 ft). (d) Total SP electric-field amplitude along y-axis. All calculations are representative of State 1 on January 26, 2022. See Fig 9 for DGFD model assumptions.

Streaming Potential Laboratory Experiments

To further evaluate the important of SP in explaining our data, we conducted preliminary SP laboratory experiments using gravity-induced water flow through a stacked EAP and sand pack (**Fig. 13**). Flow rates were controlled by maintaining the hydraulic head above the grain pack and estimated as 0.13 mL/s throughout the flow interval. The water conductivity was 0.00017 S/m. To eliminate motoelectric effects due to EAP contact with electrodes, we recessed the electrodes.

An immediate SP response was recorded with a single-step flow-rate change. We observed similar maximum SP magnitudes in sand and EAP. However, the sand interval reached a steady potential-difference value almost immediately, while the EAP interval took about 30 minutes to get to the steady state. When the flow ceased, the sand pack returned to its original potential almost immediately, and the EAP pack took a much longer time (about 1.5 hours) to return to the pre-injection state.

(a)

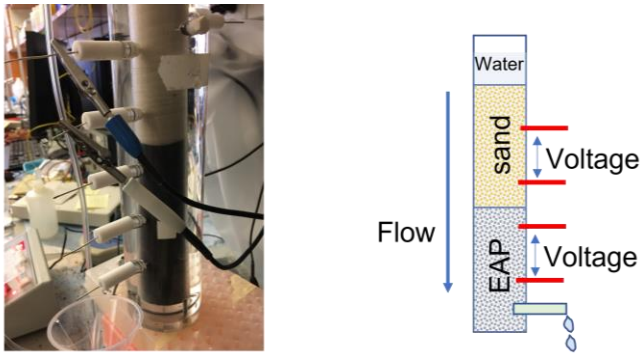

(b)

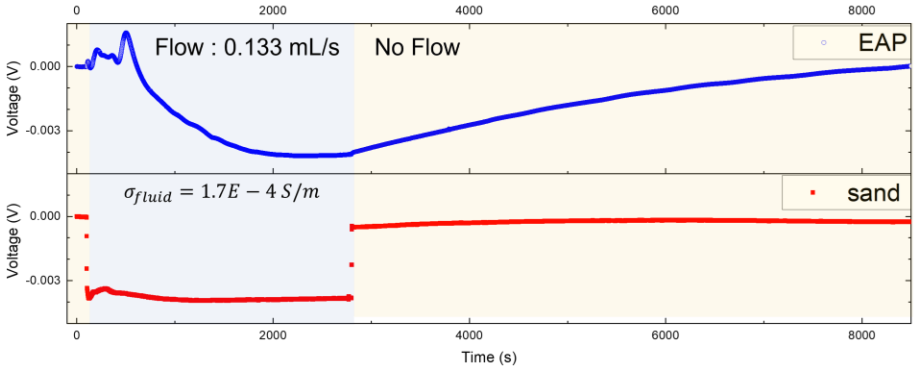

Fig. 13—(a) The experimental setup image and a schematic diagram, without a transmitter, to measure the SP. (b) Temporal change of the recorded voltage along EAP and sand granular material intervals induced by the fluid flow at rates between 0.13 and 0 ml/s.

We hypothesize that a similar transition of the states between flowing and non-flowing conditions contributes to a large portion of the observed electric field changes during State 1 for all of the injection cycles. On the other hand, the EM response, due to the increased contact resistance in the EAP pack in a larger dilated fracture zone, could play a more significant role during State 2 (Table 4).

Discussions

Our initial goal was to demonstrate that EAP-filled fracture dynamics can be detected in a surface CSEM survey in real-time due to electrical conductivity changes. The presented results support our original hypothesis about the possible usefulness of EAP in delineating the dynamics of the subsurface fluid flow. They also clearly demonstrate CSEM's ability to measure fluid flow in real time.

From plotting the surface electric potential differences combined with flow rate, salinity, and BHP during January 23, 26, and 27, we observe 1) a clear correlation between flow rate and electric potential differences in several receivers; 2) the effect of fracture dilation (inferred from the exceedance of the BHP beyond the FCP) that is more important than the salinity changes effect on the electric field during the small saltwater injection on January 27; and 3) small salinity effects on January 27. Considering multiple parallel resistivity paths for the transmitter current, the reduced resistivity of the invasion zone due to saltwater presence can lead to increased electric

current flow through the invasion zone and consequently, time-varying electric current. Thereby, although the invasion zone resistivity decreases, the increase of electric current can compensate this resistivity drop, leading to an increased recorded potential on the surface.

Our results also reveal a quite significant SP contribution to the observed field responses. This was supported by the clear correlation between the scattered electric field and the flow-rate profile during the injection initiation with negligible injected fluid volumes, when no appreciable volume of EAP could have been dilated (Fig. 12). Yet, the electric field was near its maximum (see Interval 1 in Figs. 6-7). The resulting pressure changes can influence the electric field through the SP as formulated by the coupled flow theory (De Groot and Tolhoek, 1951) and elaborated above in Eqs. 4 and 5. Based on the occurrence of the maximum pressure gradient despite small flow rates at early times, Eq. 5 leads to large spatial pressure gradients. These pressure gradients as the source term in Eq. 4 result in large SP. Hence, SP likely dominates the observed surface electric potential difference at early times. A similar trend was observed during the shut-in period, albeit more gradually when the flow rate suddenly stopped at State 3. The comparison of the electrical potential-difference traces shown in Figs. 6 and 7 with the laboratory EAP SP results (Fig. 13) demonstrates similar trends, specifically during the early-time sharp increase and the subsequent gradual decline of the voltage along the EAP interval. The contribution of EM may be more important during fracture dilation and compaction. This is supported by a smaller mismatch between EM simulations and field data in States 2 and 3.

Another possibility to explain the Interval 1 results is the rush of trapped wellbore water into the EAP-filled fracture, that was compacted due to the vacuum pore pressure developed while the wellhead valve was closed. This could have resulted in the separation of the EAP grains during this early time. We are currently in the process of conducting additional EM modeling to simulate the case when approximately 145 gallons of water rushes into the proppant pack during Interval 1.

It should be noted that matching the measured scattered field by either an analytical solution for SP, 3D EM modeling, or the sum of both was not currently achievable for the entire injection interval. Our work is in progress to perform a more accurate numerical modeling of the SP and EM responses by coupling 3D poroelastic, SP, and EM models. Because of the presence of the conductivity term in the SP Poisson's equation (Eq. 5), an indirect effect of conductivity changes on the total recorded electric field is present in the SP. This effect is in addition to the direct effect of the conductivity changes on the normal EM field disturbance. To the best of our knowledge, the current literature lacks a numerical forward model to simulate these two effects together. Developing this forward model would be critical not only for the evaluation of the causative mechanisms for the EM field observations but also for the formulation of an inverse model to achieve an accurate visualization of conductivity response during subsurface fluid injection studies.

A scattered electric field can be induced by changes in the subsurface electric conductivity, magnetic permeability, or dielectric permittivity. The mismatch between the EM simulation results and the field data may partially originate from neglected material properties that contribute to complex effects like the induced polarization (IP) response. Although not discussed in detail, the CSEM method used here captured a considerable phase response sensitivity and the quickest

change could be observed early during injection times (see Table 2). Generally, EM simulations are governed by the effective permittivity, $\tilde{\varepsilon} = \varepsilon'(\omega) - i(\varepsilon''(\omega) + \sigma/\omega)$, where the combined term $\varepsilon'(\omega) - i\varepsilon''(\omega)$ is called $\varepsilon(\omega)$ or the dielectric permittivity, σ denotes the direct-current (DC) conductivity contributing to the apparent loss, j equals $\sqrt{-1}$, and ω is the transmitter electric current frequency. $\varepsilon'(\omega)$ is expressed as $\varepsilon_0\epsilon_r$, where ϵ_r is the relative dielectric constant. In our Devine case, $\varepsilon'(\omega)$ is assumed to be 10^{-11} to 10^{-10} F/m, σ is 10^{-2} to 10^{2} S/m, ω is 10^{1} to 10^{2} $1/s$, and $\varepsilon''(\omega)$ is assumed negligible. These values lead to the dominance of the conductivity term (-σ/ω). On the other hand, low-frequency effects such as IP can be significant for an EAP material and may contribute to phase measurements.

Conclusions

Our laboratory experiments demonstrated that pressure changes within an electrically active proppant (EAP) pack can result in detectable electrical conductivity changes. We evaluated this finding in a field experiment using several high-pressure injections into a preexisting EAP-filled hydraulic fracture at the Devine Fracture Pilot Site. These injections were accompanied by surface electric potential-difference recordings during controlled-source EM (CSEM) surveys. These recordings demonstrated a strong correlation between flow rate, fracture dilation, EAP pack compaction, and electric potential difference. The observed electric potential changes during the injection of small volumes of 2500 ppm saltwater further support the ability of the CSEM to measure small conductivity changes in real time.

Our electromagnetic models based on only conductivity changes led to a large data mismatch compared to the surface recorded electric field, especially at early times of injection. We attribute this large mismatch to the absence of physics of streaming potential in our model. This is supported by the correlation between the electric potential difference during the early times of injections and an analytical solution for the SP. According to our understanding, this paper is one of the first to demonstrate the importance of the combined effects of SP and EM in a subsurface fluid-flow field case.

We believe that SP plays a major contribution to the observed electric field variations during this study. Saltwater can be used as a tracer for delineating the extent of the injected fluid boundaries. We are currently evaluating the saltwater profile and DAS data collected during these studies to substantiate these observed electric field variations. By comparing various injection cycles, we intend to deconvolute the contribution of salinity changes, the EAP-filled fracture dilation, and flow-rate induced SP to the total observed field variations. This deconvolution will be conducted by coupling SP and EM models for obtaining more accurate forward and inverse solutions to help interpret EM geophysical surveys. Because of the direct effect of spatiotemporal pore-pressure gradients and conductivity changes on the SP and EM field, the corresponding models will also need to be coupled with hydrogeomechanical models. The enhanced model and surface-based real-time CSEM method will be adopted for various subsurface applications, where monitoring fluid flow is important.

Acknowledgement

We acknowledge the U.S. Department of Energy, Office of Fossil Energy, National Energy Technology Laboratory to grant an award with Number DE-FE0031785, and the State of Texas Advanced Oil and Gas Resource Recovery program at the Bureau of Economic Geology for the initial financial seed to start the development of the DFPS. We express our gratitude to the Advanced Energy Consortium (http://www.beg.utexas.edu/aec/), with Exxon-Mobil, Repsol, Shell, and TotalEnergies, as members. We also thank Geoprojects International, Inc. for performing the hydrological operations at the DFPS and the staff at Deep Imaging Technologies for conducting the electromagnetic survey. Publication authorized by the Director, Bureau of Economic Geology, The University of Texas at Austin.

References

Ahmadian, M., D. LaBrecque, Q.H. Liu, A. Kleinhammes, P. Doyle, Y. Fang, G. Jeffrey, and C. Lucie. 2019. Validation of the utility of the contrast-agent-assisted electromagnetic tomography method for precise imaging of a hydraulically induced fracture network. In Proceedings of the SPE Annual Technical Conference and Exhibition, Calgary, Alberta, Canada, 30 September–2 October 2019. SPE-196140-MS. https://doi.org/10.2118/196140-MS.

Ahmadian, M., D. LaBrecque, Q.H. Liu, W. Slack, R. Brigham, Y. Fang, K. Banks, Y. Hu, D. Wang, and R. Zhang. 2018. Demonstration of proof of concept of electromagnetic geophysical methods for high resolution illumination of induced fracture networks. In Proceedings of the SPE Hydraulic Fracturing Technology Conference and Exhibition, The Woodlands, Texas, USA, 23–25 January 2018. SPE-189858-MS. https://doi.org/10.2118/189858-MS.

Busing, H., C. Vogt, A. Ebigbo, and N. Klitzsch. 2017. Numerical study on CO_2 leakage detection using electrical streaming potential data. *Water Resources Research* **53**: 455-469. https://doi.org/10.1002/2016WR019803.

de Groot, S.R. and H.A. Tolhoek. 1951. On the electrochemical potential. Recueil des Travaux Chimiques des Pays-Bas, 70(5): 419-420.

Denison, J., L. Murdoch, D. LaBrecque, and W. Slack. 2015. Electrical and magnetic imaging of proppants in shallow hydraulic fractures. In Proceedings of AGU Fall Meeting, San Francisco, California, USA, 14–18 December 2015. NG-13A-1872.

Fang, Y., J. Dai, Q. Zhan, Y. Hu, M. Zhuang, and Q.H. Liu. 2019. A hybrid 3D electromagnetic method for induction detection of hydraulic fractures through a tilted cased borehole in planar stratified media. *IEEE Geoscience and Remote Sensing Letters* **15**(7): 996–1000. https://doi.org/10.1109/TGRS.2019.2891674.

Fang, Y., Y. Hu, Q. Zhan, D. Wang, R. Zhang and Q.H. Liu. 2020. A fast numerical method for the galvanic measurement in hydraulic fracture detection. *IEEE Transactions on Antennas and Propagation* **68**(2): 947-957. https://doi.org/10.1109/TAP.2019.2940591.

Fitterman, D.V. 1979. Calculations of self-potential anomalies near vertical contacts. *Geophysics* **44**(2): 195-205. https://doi.org/10.1190/1.1440961.

Haddad, M., M. Ahmadian, J. Ge, J.-P. Nicot, and W. Ambrose. 2023. Geomechanical and hydrogeological evaluation of a shallow hydraulic fracture at the Devine Fracture Pilot Site, Medina County, Texas. *Rock Mechanics and Rock Engineering*, (Accepted on 11/10/2022). https://doi.org/10.1007/s00603-022-03115-z

Haddad, M., M. Ahmadian, J. Ge, S. Hosseini, J.-P. Nicot, and W. Ambrose. 2021. Hydrogeological and geomechanical evaluation of a shallow hydraulic fracture at the Devine Fracture Pilot Site, Medina County, Texas. In Proceedings of the 55th U.S. Rock Mechanics / Geomechanics Symposium, online, 20-23 June 2021. ARMA-21-1958.

Haddad, M. and Ahmadian, M. 2023. Pressure Transient Analyses and Poroelastic Modeling of Hydraulic Fracture Dilation for Multiple Injection Cycles at The Devine Fracture Pilot Site. Presented at the SPE Hydraulic Fracturing Technology Conference and Exhibition, The Woodlands, Texas, USA, 31 January-2 February. SPE-212362-MS.

Haustveit, K., K. Dahlgren, H. Greenwood, T. Peryam, and B. Kennedy. 2017. New age fracture mapping diagnostic tools-A STACK case study. In Proceedings of the SPE Hydraulic Fracturing Technology Conference and Exhibition, The Woodlands, Texas, USA, 24-26 January 2017. SPE-184862-MS. https://doi.org/10.2118/184862-MS.

Heagy, L.J., D.W. Oldenburg, and J. Chen. 2014. Where does the proppant go? Examining the application of electromagnetic methods for hydraulic fracture characterization. GeoConvention 2014: *FOCUS*. Available at: https://cseg.ca/assets/files/resources/abstracts/2014/334_GC2014_Where_does_the_proppant_go.pdf (accessed August 10, 2022).

Hu, Y., Y. Fang, D. LaBrecque, M. Ahmadian, and Q.H. Liu. 2018. Reconstruction of high-contrast proppant in hydraulic fractures with galvanic measurements. *IEEE Transactions on Geoscience and Remote Sensing* **56**(4): 2066–2073. DOI: 10.1109/TGRS.2017.2773080.

Hu, Y., Z. Yu, W. Zhang, Q. Sun, and Q.H. Liu. 2016. Multiphysics coupling of dynamic fluid flow and electromagnetic fields for subsurface sensing. *IEEE Journal on Multiscale and Multiphysics Computational Techniques* **1**: 14–25. https://doi.org/10.1109/JMMCT.2016.2559509.

Ishido, T., H. Mizutani, and K. Baba. 1983. Streaming potential observations, using geothermal wells and in situ electrokinetic coupling coefficients under high temperature. *Tectonophysics* **91**: 89-104. https://doi.org/10.1016/0040-1951(83)90059-8.

LaBrecque, D., R. Brigham, J. Denison, L. Murdoch, W. Slack, Q.H. Liu, Y. Fang, J. Dai, Y. Hu, and Z. Yu. 2016. Remote imaging of proppants in hydraulic fracture networks using electromagnetic methods: Results of small-scale field experiments. In Proceedings of the SPE Hydraulic Fracturing Technology Conference, The Woodlands, Texas, USA, 9–11 February 2016. SPE-179170-MS. https://doi.org/10.2118/179170-MS.

Malama, B. 2014. Theory of transient streaming potentials in coupled unconfined aquifer-unsaturated zone flow to a well. *Water Resources Research* **50**: 2921-2945. https://doi.org/10.1002/2013WR014909.

Mizunaga, H. and T. Tanaka. 2015. Three-dimensional inversion of fluid flow electromagnetic method to visualize geothermal fluid flow. In Proceedings of the World Geothermal Congress 2015, Melbourne, Australia, 19-25 April 2015. Available at: https://citeseerx.ist.psu.edu/viewdoc/download?doi=10.1.1.1037.4285&rep=rep1&type=pdf (accessed August 10, 2022).

Munoz, G. 2014. Exploring for geothermal resources with electromagnetic methods. *Surv Geophys* **35**: 101-122. https://doi.org/10.1007/s10712-013-9236-0.

Nobes, D.C. 1996. Troubled waters: Environmental applications of electrical and electromagnetic methods. *Surveys in Geophysics* **17**: 393-454.

Sill, W.R. 1983. Self-potential modeling from primary flows. *Geophysics* **48**: 76-86. https://doi.org/10.1190/1.1441409.

Spies, B.R. 1992. Survey design considerations for cross-well electromagnetics. *SEG Technical Program Expanded Abstracts* **1992**: 498-501. https://doi.org/10.1190/1.1822129.

Stolyarov, S., E. Cazeneuve, K. Sabaa, D. Katz, and J. Yang. 2019. A novel technology for hydraulic fracture diagnostics in the vicinity and beyond the wellbore. In Proceedings of the SPE Hydraulic Fracturing Technology Conference and Exhibition, The Woodlands, Texas, USA, 5–7 February 2019. SPE-194373-MS. https://doi.org/10.2118/194373-MS.

Sun, Q., R. Zhang, and Y. Hu. 2021. Domain decomposition-based discontinuous Galerkin time-domain method with weighted Laguerre polynomials. *IEEE Transactions on Antennas and Propagation* **69**(11): 7999-8002. https://doi.org/10.1109/TAP.2021.3076566.

Tarasov, A. and K. Titov. 2013. On the use of the Cole-Cole equations in spectral induced polarization. *Geophysical Journal International* **195**: 352-356. https://doi.org/10.1093/gji/ggt251.

Zhang, L., Z. Wang, Y. Zhu, Z. Liu, Y. Yao. 2021. The use of controlled source EM method to monitor hydraulic fracturing. In Proceedings of the SEG/AAPG/SEPM First International Meeting for Applied Geoscience & Energy, Denver, Colorado, USA and online, September 2021. https://doi.org/10.1190/segam2021-3581167.1.

Zhang, R. et al. 2022. Accelerating hydraulic fracture imaging by deep transfer learning. *IEEE Transactions on Antennas and Propagation* **70**(7): 6,117-6,121. https://doi.org/10.1109/TAP.2022.3161325.

Zhang, R. et al. 2022. Imaging hydraulic fractures under energized steel casing by convolutional neural networks. *IEEE Transactions on Geoscience and Remote Sensing* **58**(12): 8,831-8,839. https://doi.org/10.1109/TGRS.2020.2991011.

Zhdanov, M.S., M. Endo, N. Black, L. Spangler, S. Fairweather, A. Hibbs, G.A. Eiskamp, and R. Will. 2013. Electromagnetic monitoring of CO2 sequestration in deep reservoirs. *first break* **31**(2): 85-92. https://doi.org/10.3997/1365-2397.31.2.66662.